Ti-6Al-4V to over 1.2 TPa: Shock Hugoniot experiments, math xmlns="http://www.w3.org/1998/Math/MathML">mrow>mi>a/mi>mi>b/mi>/mrow>mo> /mo>mrow>mi>i/mi>mi>n/mi>mi>i/mi>mi>t/mi>mi>i/mi>mi>o/mi>/mrow>/math> calculations, and a broad-range multiphase equation of state

Pat Kalita, Kyle R. Cochrane, Marcus D. Knudson, Tommy Ao, Carrie Blada, Jerry Jackson, Jeffry Gluth, Heath Hanshaw, Ed Scoglietti, and Scott D. Crockett

Phys. Rev. B **107**, 094101 — Published 1 March 2023

DOI: 10.1103/PhysRevB.107.094101

Ti-6Al-4V to over 1.2 TPa: Shock Hugoniot experiments, ab-initio calculations and a broad-range multiphase equation of state

Pat Kalita, Kyle R. Cochrane, Marcus D. Knudson, Tommy Ao, Carrie Blada,

Jerry Jackson, Jeffry Gluth, Heath Hanshaw, Ed Scoglietti

Sandia National Laboratories, Albuquerque, NM 87125

and

Scott D. Crockett

Los Alamos National Laboratory, Los Alamos, NM 87545

Titanium alloys are used in a large array of applications. In this work we focus our attention on the most used alloy: Ti-6Al-4V (Ti64) which has excellent mechanical and biocompatibility properties with applications in aerospace, defense, biomedical and more. Here we present high-fidelity experimental shock compression data measured on Sandia's Z machine. We extend the principal shock Hugoniot for Ti64 to more than threefold compression, up to over 1.2 TPa. We use the data to validate our ab initio molecular dynamics (AIMD) simulations, and to develop a highly reliable, multiphase Equation of State (EOS) for Ti64, spanning a broad range of temperature and pressures. The first-principles simulations show very good agreement with Z data and with previous three stage gas gun data from Sandia's STAR facility. The resulting principal Hugoniot and the broad range EOS and phase diagram up to 10 TPa and 10^5 K are suitable for use in shock experiments and in hydrodynamic simulations. The high-precision experimental results and high-fidelity simulations demonstrate that the Hugoniot of the Ti64 alloy is stiffer than that of pure Ti and reveal that Ti64 melts on the Hugoniot at a significantly lower pressure and temperature than previously modelled.

1. Introduction

a. Ti-6Al-4V properties and applications

Unraveling the structure-property-performance relationship of metal alloys subjected to high-pressure and high-temperature conditions is of fundamental importance in the field of condensed matter physics, with numerous technological applications. Appearing in the USA in 1954, Ti-6Al-4V (Ti 90wt% - Al 6wt% - V 4wt%), also called Ti64, remains the most used of titanium alloys in commercial and in industrial applications. It displays excellent mechanical (high strength-to-weight ratio, high fatigue resistance, etc.), biocompatibility properties and outstanding corrosion resistance together with ease of machinability [1]. Thanks to its reliable performance Ti-6Al-4V possesses a range of applications in aerospace, automotive, biomedical (protheses and implants) as well as in chemical plant, power generation, oil and gas extraction, sporting goods, and building applications [1].

Pure titanium crystallizes in the α *hcp* lattice (hexagonal closed packed, structure: space group 194, $P6_3/mmc$) at low and ambient temperature, while at high temperature (1,155 K) it transitions to a β *bcc* lattice (body centered cubic, structure: space group 229, $Im\text{-}\bar{3}m$). The Ti-6Al-4V alloy is a two-phase alloy of titanium with substitutional aluminium and vanadium. At ambient conditions, Ti64 crystallizes predominantly in the *hcp* lattice, or α phase, but with a smaller fraction by volume of bcc or β phase Ti64 around the α grain boundaries. In Ti64 the inclusion of aluminium stabilizes the α phase while the β phase is stabilized by vanadium. Stabilization occurs by rising/lowering the transition temperature to the β phase through addition of Al/V, respectively. Hence the material is sometimes called an α + β Ti alloy [1, 2]. Alloying of the substitutional elements Al and V increases the strength of Ti64 compared to pure titanium [3].

For applications at extreme conditions such as defense, aerospace, or nuclear industries, it is paramount to have a good description of the mechanical response of the Ti64 alloy to extreme pressures and temperatures. Yet, the ubiquitous Ti64 alloy is much less studied, compared with the many investigations on pure Ti, including static and shock compression (see for example the book chapter by N. Velisavlijevic and references therein [4]).

The Ti64 Hugoniot was only examined in a few shock compression works up to 250 GPa, with most publications focusing on the region up to ~20 GPa: Rozenberg et al. measured the Hugoniot up to 14 GPa with manganin gauges [5]. Dandekar et al. [6] as well as Hopkins and Brar [7] explored the Hugoniot elastic limit up to 13 GPa. Andriot *et al*. measured the Hugoniot up to 64 GPa with velocimetry [8]. Winfree et al. extended the Hugoniot EOS of Ti-6Al-4V up to 250 GPa with shock experiments on a 3-stage gas gun [9]. Recent works have focused on Ti64 under static compression in a diamond anvil cell [10-12] including high pressure and temperature measurements [13].

The Equation of State (EOS) of a material plays a key role in describing how the material changes volume and temperature during compression. The Hugoniot, in turn, is a key parameter for describing shock compression of a material and therefore a particularly important component of building analytical EOS models. The scarcity of shock compression experimental data above 250 GPa is a limiting factor for developing a truly predictive Ti64 model. In the absence of adequate experimental data to further understand the high-pressure response of this metal alloy, an equation of state (EOS) for Ti64 cannot be constrained and validated.

Here we show, through high precision shock experiments and high-fidelity simulations, that the shock response of Ti64 is stiffer than in pure Ti and that the melting point on the Hugoniot is at a lower pressure and temperature than previously assumed. We present experimental measurements of the principal Hugoniot of Ti-6Al-4V on shock compression up to 1.27 TPa (or 1,270 GPa) using the Sandia Z machine. We couple experimental data with Ab-initio molecular dynamics (AIMD) simulations, as well as we develop a new broad range, multi-phase SESAME equation of state and phase diagram up to 10 TPa and 10^5 K. This EOS table is suitable for use in shock experiments and in hydrodynamic simulations requiring a high-accuracy EOS description of Ti64.

b. Shock compression

Shock compression is the primary method for exploring the extreme thermodynamic states of stress and temperature. A single shock compression experiment consists of the measurement of a material's

end state achieved by single shock wave compression at constant velocity, from a given initial (ambient) state. In a simple shock experiment the conservation of mass, momentum, and energy is described by Rankine-Hugoniot jump conditions [14, 15] (Eqs. 1-3), where P, ρ and E are the pressure, density, and specific internal energy, respectively, of the shocked material relative to its initial state, denoted with the subscript 0. P, ρ, and E are related by the shock velocity (U_S) and particle velocity behind the shock front (U_P) of the shock wave.

$$\frac{\rho}{\rho_0} = \frac{U_S}{U_S - U_P} \quad \text{(Eq. 1)}$$

$$P - P_0 = \rho_0 U_S U_P \quad \text{(Eq. 2)}$$

$$2(E - E_0) = (P + P_0)\left(\frac{1}{\rho_0} - \frac{1}{\rho}\right) \quad \text{(Eq. 3)}$$

The 'Hugoniot' is then defined as a collection of loci of material end states achieved from a given initial state, and in practice it is a collection of P-ρ data points or U_S - U_P data points. By definition, the 'Principal Hugoniot' initiates from ambient conditions, while non-ambient initial conditions lead to measuring 'off-Hugoniot' states. To describe the Hugoniot from a collection of single shock experiments one must measure 2 out of the 5 unknown quantities: U_P, U_S, ρ, P, or E. Typically the easiest to measure in a shock experiment is either U_P, or U_S, but both cannot be measured in one experiment (except in the special case of a symmetric impact, where the sample and the impactor are made of the same material). Instead, one can use a process in which a well-characterized standard material with a known Hugoniot (Al, Ta etc.) is used as the impactor material. This allows one to infer the pressure and density of the material of interest: this is called impedance matching with a standard [16]. Current impedance matching techniques utilize Monte Carlo algorithms to propagate uncertainties in Hugoniot states by incorporating all random experimental uncertainties as well as systematic uncertainties from the standard. The process of Monte Carlo impedance matching is detailed in the following section.

2. Experiments on the Z machine, VISAR, data processing and analysis

We carried out shock compression experiments using the Sandia National Laboratories' Z Machine [17]. The Z machine is a pulsed power system capable of producing shaped current pulses and inducing magnetic fields of more than 20 MA and 10 MG, respectively. One can utilize the Z machine to accelerate aluminum flyer plates up to 40 km/s [18] to probe shock Hugoniot states. In this study, the highest velocity achieved was 30.8 km/s. In the present experiments, we generated shocked states from 0.21 TPa up to 1.27 TPa (210 GPa to 1270 GPa) using the two geometries illustrated in Figure 1: the coaxial geometry and the 2-sided stripline geometry for extremely high velocity experiments. The Al flyer plate was shocklessly accelerated toward the target stack composed of a sample of Ti-6Al-4V Grade 5 (Ti-6Al-4V, Grade 5 per ASTM B 348, Al=6.24 wt%, V=3.97wt.%, 300-500 μm thickness depending on experiment, 4.43 g/cm^3) and an alpha-quartz window. While the back side of the flyer was melted by the high driving current, the impact side of the flyer remained at solid density [18], producing a steady shock in the sample upon impact. For example, in the highest

pressure shot, the flyer thickness was 1050 ns and the experiment was designed to produce at least 20 ns of steady shock wave, while the actual transit time through the sample was less than 20 ns.

We used two, push-pull velocity interferometer system for any reflector (VISAR, [19, 20]) systems with dual velocity per fringe (VPF) capabilities to measure velocity of the flyer plate from rest up to impact with the target (Fig. 1). Three VISAR signals were typically recorded for the sample eliminating ambiguities and providing redundant measurements for improved precision. Typically, three different VPFs were used on each sample and each window above or below the sample, for example: 0.5878 km/s/f, 1.0632 km/s/f, and 1.4317 km/s/f.

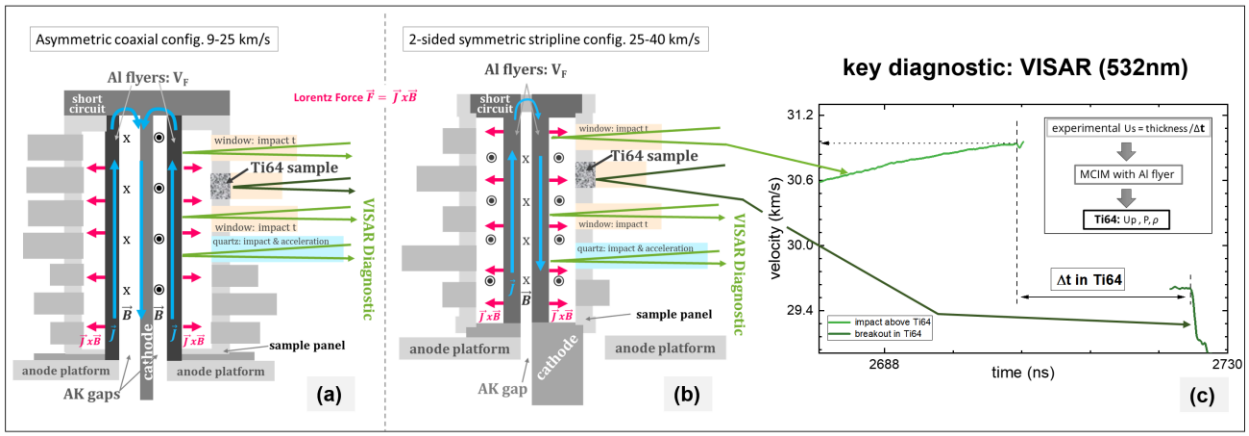

Figure 1. A shock compression experiment on the Z machine. (a) Schematic of the asymmetric coaxial load configuration for lower velocity experiments and (b) that of the 2-sided symmetric stripline configuration for high velocity experiments, illustrating how flyer acceleration is produced and the need for multiple VISAR signals. (c) Representative measured VISAR signals from one of the high velocity experiments on Ti64, and the workflow to obtain a Hugoniot point from the measured quantity Δt.

Since the sample is opaque to VISAR light, impact time was determined from fiducials observed in transparent windows adjacent to the opaque sample stack. Impact time was then corrected for any measured tilt of the impact plane and for the relative offset of the 2 windows as compared to the opaque sample (typically a few microns). Shock breakout was directly monitored at the back surface of the opaque sample, through a window. The sample shock velocity (U_S) was calculated using the transit time determined from the VISAR fiducials and the measured thickness. The shock wave was also monitored in a thick quartz witness window, which allowed us to determine any necessary correction due to acceleration of the flyer and apply this correction to the U_S of the sample. For the transit time measurements, the uncertainty was typically less than 0.5%. In the VISAR analysis, we determined the shock velocity via the transit time using unprocessed VISAR signals. To calculate transit time, we determined when the raw VISAR signal exhibited a change larger than the standard deviation of the signal prior to the change. That marked the impact and the transit into the backing window. The standard deviation from the transit time determination and the uncertainty in the sample thickness was used to determine the uncertainty in the shock velocity. The initial densities of the Ti64 sample and Al flyer plate, the measured flyer velocity at impact (V_F), and the inferred U_S of the sample, enables calculation of the sample Hugoniot state density (ρ), pressure (P), and particle

velocity (U_P). The Hugoniot state was determined using a Monte Carlo impedance matching analysis [21, 22] to solve the Rankine-Hugoniot equations (Eqs. 1-3) [15]. The Monte Carlo impedance matching (MCIM) method accounts for the correlated and uncorrelated uncertainties in the experimental measurement and the Al Hugoniot standard. In the MCIM, uncorrelated random numbers with one standard deviation equal to the measurement uncertainty were used to perturb the flyer velocity, the shock velocity, and the initial densities about their mean values. Correlated random numbers were used to perturb the fit parameters for the aluminum Hugoniot standard. The linear fit parameters and correlation between the parameters used for the aluminum standard are listed in Table I. The impedance matching calculation was performed to determine U_P, ρ and P in the Hugoniot state. The data were saved, and the calculation restarted using new random numbers. A database of Hugoniot states was built for 10^7 iterations and the final Hugoniot state was calculated as the mean with 1-standard deviation of the distribution as the uncertainty. The experimentally determined Hugoniot states with uncertainties are listed in Table II.

Table I. Aluminium flyer plate Hugoniot linear fit parameters and covariance matrix parameters for $U_S = C_0+S_1U_P$

Flyer	C_0 (km/s)	S_1	σ^2_{C0} x 10^3	σ^2_{S1} x 10^3	$\sigma_{C0}\sigma_{S1}$ x 10^3
Al	6.322 ± 0.231	1.188 ± 0.020	53.58	0.4195	-4.605

Table II. Experimental data for the principal Hugoniot of Ti-6Al-4V. The initial density was 4.43 g/cm^3 with an uncertainty of 0.3%.

Flyer	V_F (km/s)	U_P (km/s)	U_S (km/s)	ρ (g/cc)	P (GPa)
Al	10.50 ± 0.02	4.68 ± 0.03	10.03 ± 0.04	8.31 ± 0.07	208.0 ± 2.0
Al	11.98 ± 0.04	5.30 ± 0.05	10.96 ± 0.15	8.58 ± 0.18	257.4 ± 2.8
Al	12.66 ± 0.03	5.57 ± 0.04	11.45 ± 0.07	8.63 ± 0.09	282.7 ± 2.1
Al	12.88 ± 0.01	5.68 ± 0.04	11.50 ± 0.09	8.76 ± 0.11	289.3 ± 2.2
Al	14.70 ± 0.01	6.46 ± 0.04	12.55 ± 0.09	9.13 ± 0.11	359.0 ± 3.0
Al	17.87 ± 0.02	7.79 ± 0.05	14.44 ± 0.14	9.62 ± 0.17	498.5 ± 4.1
Al	24.04 ± 0.01	10.46 ± 0.06	17.80 ± 0.12	10.75 ± 0.20	825.0 ± 6.0
Al	30.83 ± 0.06	13.43 ± 0.08	21.34 ± 0.15	11.96 ± 0.22	1270.0 ± 10.0

3. Ab initio molecular dynamics calculations

First-principles density functional theory (DFT) was used to conduct ab initio molecular dynamics (AIMD) calculations of the Hugoniot using the Vienna ab-initio simulation package (VASP) [23-26]. The AIMD simulations were performed in the canonical (NVT) ensemble with the Mermin generalization of the Kohn-Sham equations to finite temperature [27]. The exchange-correlation energy was computed with the parameterization of Perdew, Burke, and Ernzerhof (PBE) [28]. In the Kohn-Sham equations, the nuclei were represented by a projector augmented wave (PAW) method [29]. The pseudopotentials contained 3 electrons, 12 electrons, and 13 electrons for aluminum,

titanium, and vanadium respectively. The cutoff energy was set to 700 eV. The k-point mesh was Monkhorst-Pack [30] 2x2x2 for a 128 atom *hcp* reference cell. The vanadium 4 wt% and aluminum 6 wt% were rounded to an integer number of 5 and 13 atoms, which were substituted randomly into the titanium lattice (Fig. 2), because DFT is not realistically capable of looking at grain boundary effects. The vanadium 4 wt.% and aluminum 6 wt.% atoms were substituted randomly into the titanium lattice (Fig. 2) using the ATAT code [31]. Three different initial atom position configurations were tested and the difference in energy and pressure between them was negligible. We only examined the α (*hcp*) phase on the assumption that the vast majority of the material would be in this phase and the contribution to the reference state by the β (*bcc*) BCC grain boundary would be small. The simulation ran for 6 picoseconds at 0.6 fs per time step for ion motion using velocity scaling as the thermostat. The 6 g/cm^3 Hugoniot point is in the ω phase, so that simulation used 192 atoms. The higher compression simulations were in the liquid phase and used 128 atoms. Hugoniot material states were interpolated from bracketing simulations. Table III lists the calculated Hugoniot states from the present AIMD calculations.

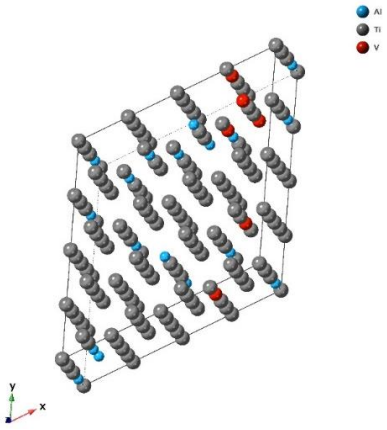

Figure 2. Representation of the crystal lattice used in the AIMD calculations: Ti: grey speres; Al: blue spheres; V: red spheres.

Table III. DFT-MD Hugoniot data for Ti-6Al-4V.

N atoms	ρ (g/cm^3)	T (K)	Pressure (GPa)	Energy (J/kg)	U_P (km/s)	U_S (km/s)
128	5.0	364.4	16.2	-1.96E+07	0.650	5.703
192	6.0	887.5	54.3	-1.82E+07	1.796	6.862
192	7.0	2860.3	110.0	-1.53E+07	3.022	8.232
128	7.5	3951.2	146.6	-1.31E+07	3.683	8.998
128	7.7	4744.4	164.0	-1.20E+07	3.968	9.343
128	8.0	6358.5	194.2	-1.01E+07	4.425	9.917
128	8.3	8409.0	228.1	-7840731	4.902	10.514
128	9.0	14912.4	334.8	-659253.9	6.197	12.204
128	10.0	30714.9	571.5	1.61E+07	8.479	15.222
128	11.0	58752.1	974.6	4.59E+07	11.464	19.195

4. Development of a broad range EOS

We developed a new EOS table in the SESAME[1] format [32], SES92966, which gives a broader range of densities and temperatures than was feasible to produce with DFT. A tabular-style EOS like SESAME is often required for many types of simulations. SESAME tables have been used in hydrodynamic calculations since the early 1970's.

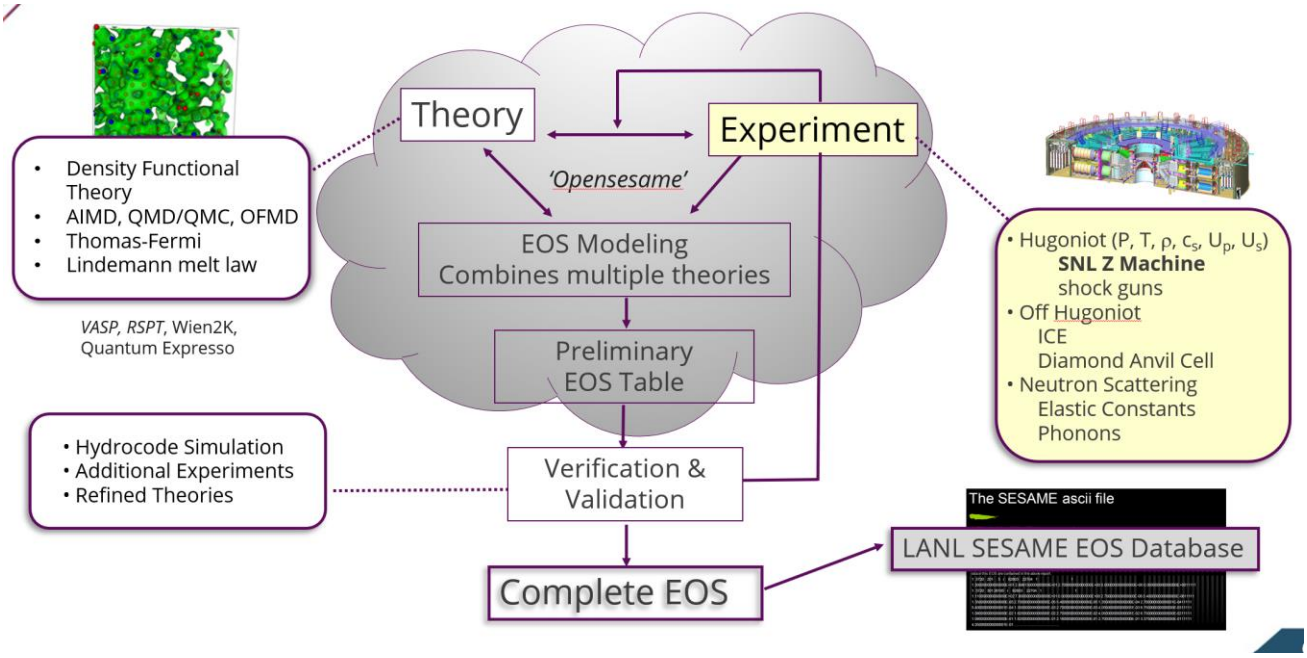

Figure 3. Workflow involved in the design of a SESAME-style equation of state.

In the development of the SESAME EOS (see Fig. 3), we used a standard three term decomposition of the Helmholtz free energy: cold curve, ion thermal, and electron thermal components, i.e., $F(T,V)=F_{cold}(V)+F_{ion}(T,V)+F_{electron}(T,V)$ [32]. The ion thermal component used a Debye approximation for the solid [33] and a corrected Debye [34] approximation for the fluid [35]. The thermodynamic Grüneisen gamma **(γ_{ref} = 1.14)** and reference Debye temperature **(θ_{ref}=318 K)** in the ion thermal model [36] were set by matching isobaric expansion data [37, 38] and specific heat [39]. The cold curve, **in the form of a Birch-Murnaghan [40]** was determined by leveraging diamond anvil cell data and density functional theory results as constraints. The derivative of the Grüneisen gamma (γ) parameter with respect to density was obtained by matching shock compression data and quantum molecular dynamic calculation in the fluid phase. The electron thermal component was determined using the Thomas-Fermi-Dirac (TFD) model. In the region of the liquid shock data, the free parameters consist of g_{ref}, q_{ref}, for the ion model and a 4th order Birch-Murnaghan cold curve.

[1] Specific SESAME EOS requests can be made via the LANL website:
https://www.lanl.gov/org/ddste/aldsc/theoretical/physics-chemistry-materials/sesame-database.php

5. Results and Discussion: experimental shock data to over 1.2 TPa, AIMD and EOS

In this section we present the results of the 3-pronged approach of this project: experimental shock data to over 1.27 TPa, AIMD modeling to the same pressure and a high-fidelity, multiphase SESAME EOS Ti64.

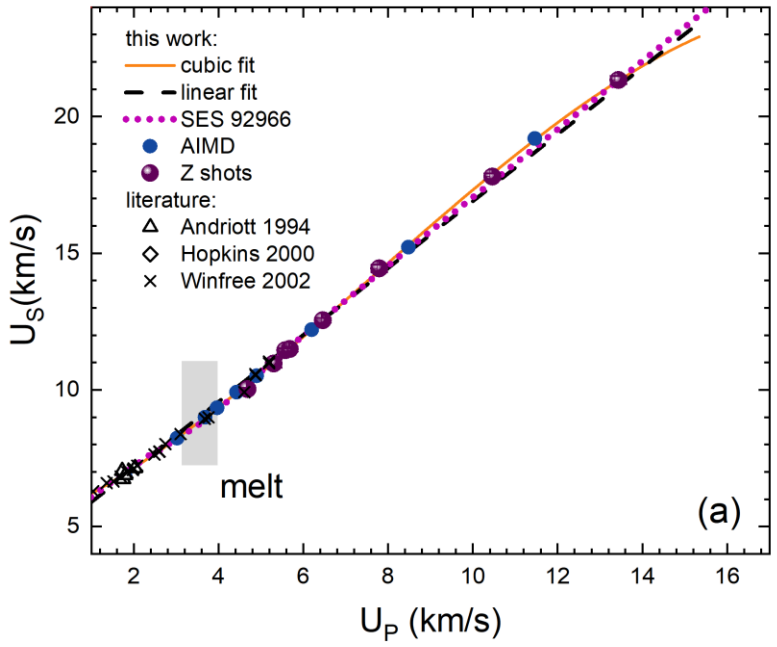

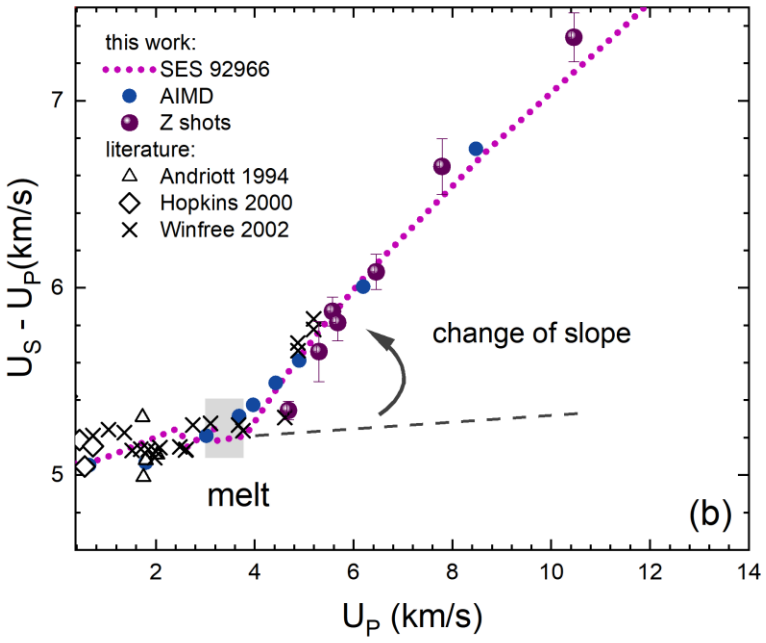

Figure 4. (a) Ti64 Hugoniot Z data in U_S - U_P space, alongside AIMD data (this work), SESAME 92966 (this work, dotted purple line) and literature gun data. Also shown are the fits to the data: linear fit (dashed black line) and cubic fit (solid orange line); **(b)** Plot of U_S-U_P versus U_P that highlights the change in slope due to shock melt. The dashed line is a guide to the eye.

The experimental Hugoniot data in U_S-U_P space from the Z machine experiment are presented in Fig. 4. The corresponding experimental P-ρ states are presented in Fig. 5. We also compare, in Fig. 5, the present Z data and AIMD simulations with: prior gun data from Hopkins [7], Andriot [8] and Winfree [9], as well as with three EOS models: the new SESAME 92966, which is developed in this work, SESAME 2970 for pure Ti [41] and SESAME 4061 for Ti64 [41]. The Z machine Hugoniot data extend from 0.21 TPa to 1.26 TPa and span a range of 3-fold compression (Fig. 4 and 5). The lowest pressure points from the Z machine (208-257 GPa) overlap with gas gun data from Winfree [9] and hence provide continuity between data from different platforms.

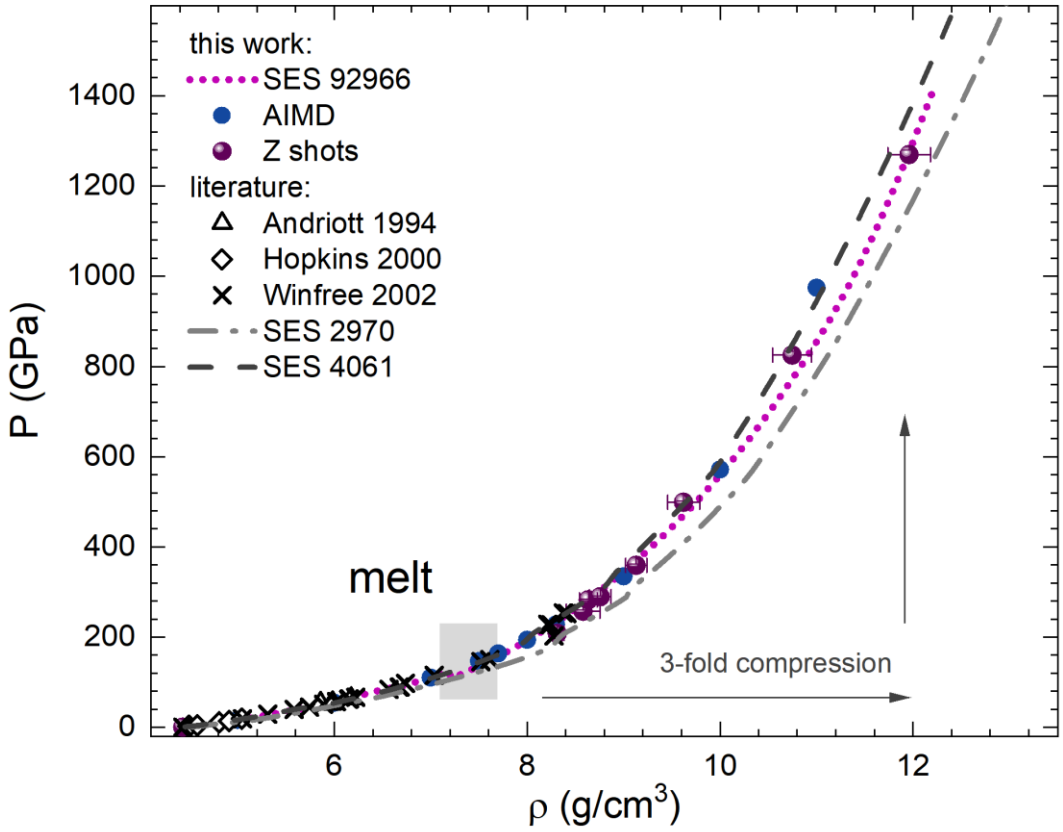

Figure 5. Ti6Al4V Hugoniot Z data in P - ρ space, alongside AIMD data and SESAME 92966 (this work), literature gun data and two SESAME EOSs: SEAME 4061 and SESAME 2970 for pure Titanium.

It is straightforward to conclude from the results in Fig. 4 and 5 that the AIMD calculations are in excellent agreement with the experimental data from Z. Because the AIMD is entirely independent from the experimental data, the agreement between theory and experiment provides a high degree of confidence in AIMD calculations. The SESAME 92966 EOS developed in this work is consistent with the Z data and the AIMD calculations, over the range covered by the experiments (Fig. 5). The high precision shock experiments and high-fidelity simulations in Fig 5 all display an increased curvature towards lower densities in P-ρ space, or stiffening in the Hugoniot with respect to pure Ti (SESAME 2970).

Examining the Hugoniot in $U_S - U_P$ space or in P – ρ space (Fig. 4-5) can be a valuable way to identify possible phase transitions, including shock melting. Examples of shock-melt in metals detectable as slight discontinuities in the Hugoniot in $U_S - U_P$ or a subtle steepening in P – ρ space are: Al [42], Fe [43], Cu [44] and V [45]. In Fig. 4(a) at $U_P \sim 3.8$ km/s we observe a discontinuity in the Hugoniot, which also appears in Fig. 5 as a subtle steepening in P - ρ space beginning at ρ ~ 7.4 g/cm³ or P ~140 GPa. This discontinuity likely arises from shock-driven melt in Ti64. It has been proposed [46] that the effects of pressure and material properties on the shock response are more easily seen and analyzed by plotting U_S-U_P versus U_P. Such a plot re-casts shock velocity in a frame of reference moving with the material behind the shock, i.e., with velocity U_P and can be very useful to highlight slope changes due to shock-melt transitions [42, 46]. Fig. 4(b) shows U_S-U_P as a function of U_P for Ti64. In Fig 4(b) we note the very clear change in slope in the region U_P ~3.8 km/s (or ρ ~7.4 g/cm³, or ~130 GPa), which we interpret as a shock-melt transition.

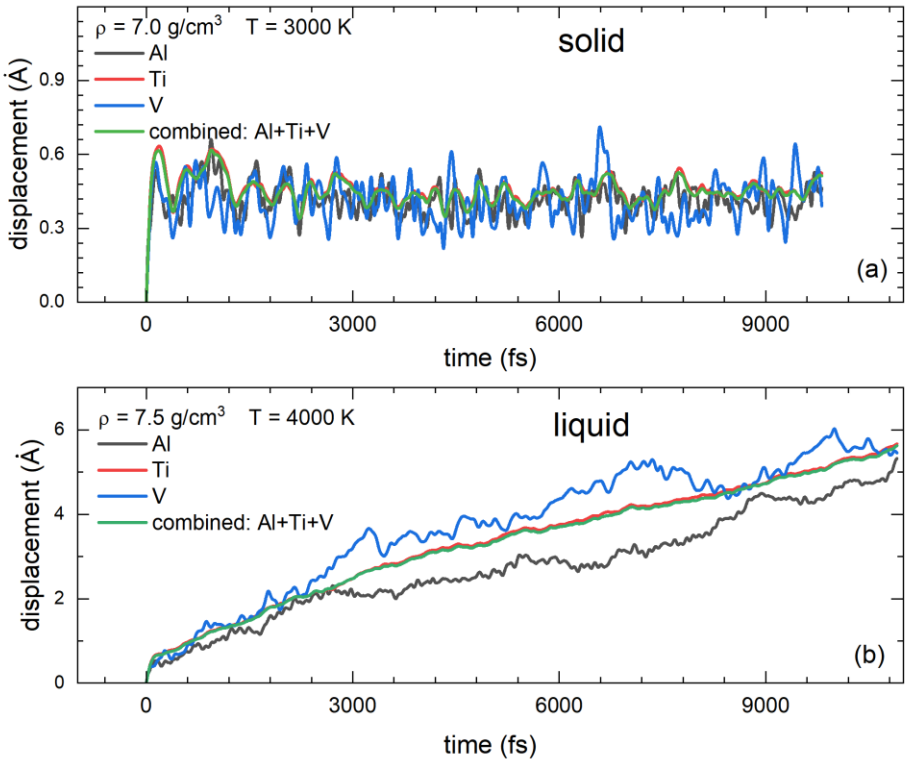

Figure 6: The mean atom displacement from two different simulations: still solid Ti64 at 7.0 g/cm³ at 3000 K (top) and Ti64 has begun to melt at 7.5 g/cm³ at 4000 K (bottom). Single species and combined displacement are shown alongside each other.

AIMD simulations were performed near melt for ρ = 7.0 g/cm³ at 3000 K and 3500K and 7.5 g/cm³ at 3700 K and 4000 K. We interpolate along temperature at constant density for each Hugoniot point. Figure 6 shows the mean atom displacement from two different simulations. The first is at 7.0 g/cm³ and 3500 Kelvin and the second is at 7.5 g/cm³ and 4000 Kelvin. These two simulations were selected

as they are at bounding temperatures of our bracketing simulations. Figure 6(a) shows the AIMD simulation at 7.0 g/cm^3 and Figure 6(b) shows 7.5 g/cm^3. As can be seen, Ti64 is solid at the lower temperature point, but has begun to melt at 4000K. Also seen in Figure 6 (b) is the species-dependent and independent displacement. The aluminum and vanadium shift as if they are a liquid and then appear remain stationary for some time before moving again. This is due to the low number of atoms (13 Al and 5 V). To test this, we calculated the displacement of the titanium in blocks of 13 atoms and saw similar behavior. When the entire simulation is assumed to be a single species (Fig. 6(b), line marked "combined Al+Ti+V"), this artifact of averaging over few atoms is no longer present. The constant increase in displacement (Fig. 6(b)) is an established signature of a liquid system.

Over the range of all the experimental data from the Z machine and from literature the U_S-U_P data exhibit a slight curvature (Fig. 4). To facilitate the use of Ti64 as an experimentally constrained impedance matching material, we fit a cubic polynomial to all experimental data:

$$U_s = C_0 + C_1 U_P + C_2 U_P^2 + C_3 U_P^3 \qquad \text{(Eq. 4)}$$

The cubic fit results are listed in Table IV and the covariance matrix elements are listed in Table V. This functional form was chosen because the cubic polynomial captures well the slight curvature in the data and the uncertainty in the fit parameters are well approximated by Gaussian distributions. This polynomial fit is only valid over the range of the experimental data. Since impedance matching with a linear U_S – U_P is often sufficient for experimental design and simulation of simple configurations, we also list a linear fit to the experimental data from the Z machine and from literature. The linear fit has the advantage of being quick and easy to implement in experiment planning and simulations. Linear fit results and the covariance matrix elements are listed in Table VI.

Table IV. Parameters for the cubic fit of the Ti64 Hugoniot: $U_S = C_0+S_1U_P + C_2U_P^2 + C_3UP^3$.

C_0 (km/s)	C_1 (km/s)$^{-1}$	C_2 (km/s)$^{-2}$	C_3 (km/s)$^{-3}$
5.411 ± 0.082	0.709 ± 0.058	0.086 ± 0.011	-0.0037 ± 5.301 x10^{-4}

Table V. Covariance matrix elements for the cubic fit parameters.

	σ_{C0}	σ_{C1}	σ_{C2}	σ_{C3}
σ_{C0}	0.0067	-0.00447	7.69223 x10^{-4}	-3.58048 x10^{-5}
σ_{C1}	-0.00447	0.00332	-6.03258 x10^{-4}	2.88611 x10^{-5}
σ_{C2}	7.69223 x10^{-4}	-6.03258 x10^{-4}	1.14434 x10^{-4}	-5.61709 x10^{-6}
σ_{C3}	-3.58048 x10^{-5}	2.88611 x10^{-5}	-5.61709 x10^{-6}	2.80993 x10^{-7}

Table VI. Ti64 Hugoniot linear fit parameters and covariance matrix elements for $U_S = C_0+S_1U_P$

C_0 (km/s)	S_1	σ^2_{C0} x 10^5	σ^2_{S1} x 10^8	$\sigma_{C0}\sigma_{S1}$ x 10^7
4.672 ± 0.058	1.223 ± 0.012	1.156	2.354	3.469

Finally, putting together the present experimental and AIMD results, in conjunction with the best available experimental data, we generate a new tabular multiphase EOS for Ti64. The overall EOS consists of the liquid phase as well as the ambient phase and the higher-pressure crystal phases. The new EOS SESAME 92966 is illustrated in Fig. 7, as a wide-ranging phase diagram of Ti64 spanning 1 TPa and 10^5 K. Fig. 7 shows the density and temperature range of the EOS table as well as the assumed phase of the material as a function of pressure and temperature. In the present SESAME 92966 the estimated onset of shock melt on the Hugoniot is ~110 GPa and ~3000 K (Fig. 7). This is in excellent agreement with the observed discontinuity in the experimental Hugoniot curve (Fig. 4). The AIMD calculations suggest that at 110 GPa the material is still in the solid state; this is consistent with the observation that DFT tends to overestimate melt temperatures [47].

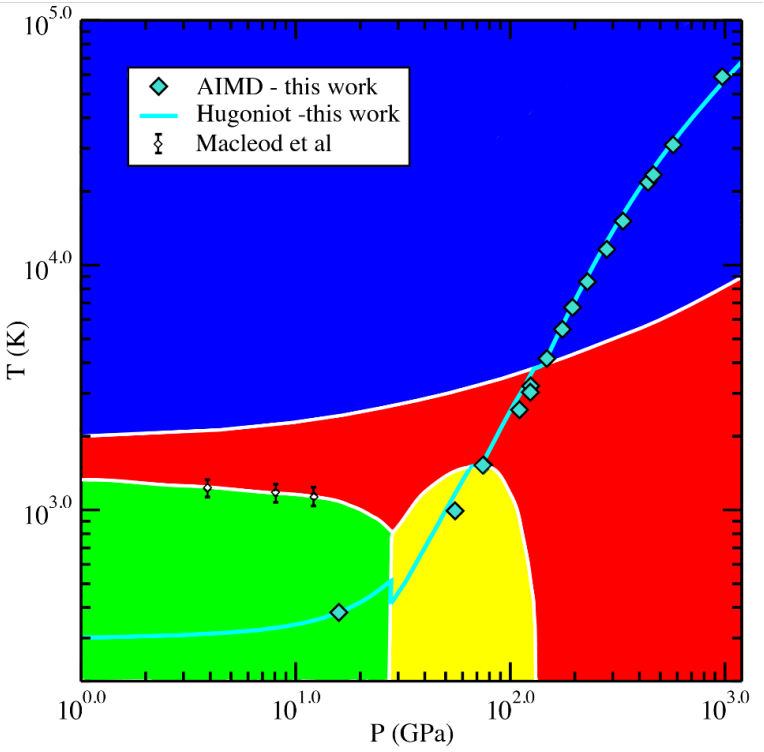

Figure 7. SESAME EOS 92966 wide-ranging phase diagram of Ti64 spanning 10 TPa and 10^5 K. The α phase is represented in green, the ω phase in yellow, the β phase in red and the liquid in blue. The solid teal curve is the principal Hugoniot with overlapped AIMD calculations (teal diamonds). The α - β phase boundary data points (hollow diamonds) are from Ref. [13].

6. Summary and Conclusions

In this work we examined the shock response of the titanium alloy Ti-6Al-4V (Ti64). New shock Hugoniot data are presented from experiments on the Sandia Z machine. The pressure ranges from 0.21 TPa up to over 1.27 TPa and corresponds to a 3-fold compression of Ti64. The AIMD calculations are in excellent agreement with the experimental data. We also developed a high-fidelity, multiphase

EOS of Ti64, SESAME EOS 92966, spanning a broad range of temperatures and pressures. The resulting Hugoniot is suitable for use in experiments as an impedance matching standard, while the new SESAME EOS is now validated with shock data up to 1.2 TPa and can be used in hydrodynamic simulations involving shock compression of solid materials. The wide-ranging SESAME EOS and phase diagram up to 10 TPa and 10^5 K accesses higher density and higher temperature regimes than the AIMD table, thereby allowing simulation of a wider variety of experiments, particularly in regimes where AIMD calculations are computationally intractable.

When comparing the Ti64 Hugoniot obtained in this work with that of pure Ti [41], it is apparent that (Fig. 5) the Ti64 Hugoniot is stiffer with respect to pure Ti, where stiffening corresponds to an increased curvature towards lower densities in P-ρ space. Previous EOS models predicted [41] a substantial stiffening of the Hugoniot in the alloy, compared to pure Ti. The present Z data and AIMD demonstrate that the stiffening does occur, but to a lesser extent, over the 3-fold compression. One can interpret the Hugoniot stiffening in the alloy by considering that, at low compression, the P(V) Hugoniot and the isentrope are close to each other. Then P(V) is proportional to $B(1-V/V_0)$ where B is the bulk modulus or incompressibility of the material. For a material with a larger bulk modulus, the Hugoniot will then be stiffer i.e., have a larger P(V) slope. The bulk modulus for the Ti64 crystal phases ranges from 120 GPa to 156 GPa [13] while pure Ti has smaller bulk moduli ranging from 110 GPa to 130 GPa [48].

Ti64 melt on the Hugoniot was previously suggested [41] to occur at 6000-6800 K and 182-207 GPa, while in pure Ti it was proposed at 6000-7000 K and 178-202 GPa, based on a thermodynamic multiphase model. That model also proposed that shock-melt of Ti64 was likely being underestimated by 10%. Here we present evidence that shock-melt of Ti64 is in fact much lower, at $\rho \sim 7.4$ g/cm^3 or ~140 GPa on the Hugoniot. Moreover, a recent experimental work [49] showed that in pure Ti the melt curve follows a much lower P and T path. In reference [49] the melt curve for pure Ti was measured experimentally in a diamond anvil cell combined with laser heating and that work reported, at 110 GPa, a range of melt temperatures of 2800-3100 K. The melt curve in Ti64 is expected to be at least similar to that of pure Ti owing to the predominance of Ti in the alloy's composition: for example, at ambient pressure Ti melts at ~1941 K and Ti64 at 1943 K [50].

Acknowledgments

The authors acknowledge the outstanding work of the Z target fabrication team and the many teams that operate and manage the Z machine. The authors are grateful to Dr. T. R. Mattsson, SNL, for a critical reading of the paper and valuable discussions.

results of federally sponsored research in accordance with the DOE Public Access Plan https://www.energy.gov/downloads/doe-public-access-plan."

Sandia National Laboratories is a multimission laboratory managed and operated by National Technology and Engineering Solutions of Sandia, LLC., a wholly owned subsidiary of Honeywell International, Inc., for the U.S. Department of Energy's National Nuclear Security Administration under Contract No. DE-NA-0003525. This paper describes objective technical results and analysis.

Any subjective views or opinions that might be expressed in the paper do not necessarily represent the views of the U.S. Department of Energy or the United States Government.

Work at LANL was supported by the US DOE through contract number 89233218NCA000001.

Literature

[1] G. Lütjering, J.C. Williams, Titanium, Springer-Verlag, Berlin Heidelberg, 2007.
[2] C. Veiga, J.P. Davim, A.J.R. Loureiro, Properties and applications of titanium alloys: a brief review., Rev. Adv. Mater. Sci., 32, 14-34 (2012).
[3] M. Peters, J. Hemptenmacher, J. Kumpfert, C. Leyens, Titanium and Titanium Alloys: Fundamentals and Applications, in: C. Leyens, M. Peters (Eds.), Weinheim: Wiley-VCH, pp. 1-35, 2003.
[4] N. Velisavljevic, S. MacLeod, H. Cynn, Titanium Alloys at Extreme Pressure Conditions, in: A.K.M.N. Amin (Ed.) Titanium Alloys - Towards Achieving Enhanced Properties for Diversified Applications, InTech 2012.
[5] Z. Rosenberg, Y. Meybar, D. Yaziv, Measurement of the Hugoniot curve of Ti-6Al-4V with commercial manganin gauges, Journal of Physics D: Applied Physics, 14, 261-266 (1981).
[6] D.P. Dandekar, S.V. Spletzer, Shock response of Ti-6Al-4V, AIP Conference Proceedings, 505, 427-430 (2000).
[7] A. Hopkins, N.S. Brar, Hugoniot and shear strength of titanium 6-4 under shock loading, AIP Conference Proceedings, 505, 423-426 (2000).
[8] P. Andriot, P. Lalle, J.P. Dejean, Quasi-elastic behavior of pure titanium and TA6V4 titanium alloy at high pressure, AIP Conference Proceedings, 309, 1009-1012 (1994).
[9] N.A. Winfree, L.C. Chhabildas, W.D. Reinhart, D.E. Carroll, G.I. Kerley, EOS Data of Ti-6Al-4V to Impact Velocities of 10.4 km/s on a Three-Stage Gun, AIP Conference Proceedings, 620, 75-78 (2002).
[10] G.N.V. Chesnut, N. & Sanchez, L. , Static High pressure X-ray Diffraction of Ti-6Al-4V., Proceedings of the American Physical Society Topical Group on Shock Compression of Condensed Matter – 2007, Kohala Coast, Hawaii, USA, pp. 27-30, 2007.
[11] I. Halevy, G. Zamir, M. Winterrose, G. Sanjit, C.R. Grandini, A. Moreno-Gobbi, Crystallographic structure of Ti-6Al-4V, Ti-HP and Ti-CP under high-pressure, Journal of Physics: Conference Series, 215, 012013 (2010).
[12] S.G. MacLeod, B.E. Tegner, H. Cynn, W.J. Evans, J.E. Proctor, M.I. McMahon, G.J. Ackland, Experimental and theoretical study of Ti-6Al-4V to 220 GPa, Physical Review B, 85, 224202 (2012).
[13] S.G. MacLeod, D. Errandonea, G.A. Cox, H. Cynn, D. Daisenberger, S.E. Finnegan, M.I. McMahon, K.A. Munro, C. Popescu, C.V. Storm, The phase diagram of Ti-6Al-4V at high-pressures and high-temperatures, Journal of Physics: Condensed Matter, 33, 154001 (2021).

[14] G.E. Duvall, R.A. Graham, Phase transitions under shock-wave loading, Reviews of Modern Physics, 49, 523-579 (1977).
[15] Y.B. Zel'Dovich, Y.P. Raizer, Physics of Shock Waves and High Temperature Phenomena, Dover Publications, Inc., Mineola, NY, 2002.
[16] M.B. Boslough, J.R. Asay, Basic Principles of Shock Compression, in: J.R. Asay, M. Shahinpoor (Eds.) High-Pressure Shock Compression of Solids, Springer New York, New York, NY, pp. 7-42, 1993.
[17] D.B. Sinars, M.A. Sweeney, C.S. Alexander, D.J. Ampleford, T. Ao, J.P. Apruzese, C. Aragon, D.J. Armstrong, K.N. Austin, T.J. Awe, A.D. Baczewski, J.E. Bailey, K.L. Baker, C.R. Ball, H.T. Barclay, S. Beatty, K. Beckwith, K.S. Bell, J.F. BenageJr., N.L. Bennett, K. Blaha, D.E. Bliss, J.J. Boerner, C.J. Bourdon, B.A. Branch, J.L. Brown, E.M. Campbell, R.B. Campbell, D.G. Chacon, G.A. Chandler, K. Chandler, P.J. Christenson, M.D. Christison, E.B. Christner, R.C. ClayIII, K.R. Cochrane, A.P. Colombo, B.M. Cook, C.A. Coverdale, M.E. Cuneo, J.S. Custer, A. Dasgupta, J.-P. Davis, M.P. Desjarlais, D.H. DolanIII, J.D. Douglass, G.S. Dunham, S. Duwal, A.D. Edens, M.J. Edwards, E.G. Evstatiev, B.G. Farfan, J.R. Fein, E.S. Field, J.A. Fisher, T.M. Flanagan, D.G. Flicker, M.D. Furnish, B.R. Galloway, P.D. Gard, T.A. Gardiner, M. Geissel, J.L. Giuliani, M.E. Glinsky, M.R. Gomez, T. Gomez, G.P. Grim, K.D. Hahn, T.A. Haill, N.D. Hamlin, J.H. Hammer, S.B. Hansen, H.L. Hanshaw, E.C. Harding, A.J. Harvey-Thompson, D. Headley, M.C. Herrmann, M.H. Hess, C. Highstrete, O.A. Hurricane, B.T. Hutsel, C.A. Jennings, O.M. Johns, D. Johnson, M.D. Johnston, B.M. Jones, M.C. Jones, P.A. Jones, P.E. Kalita, R.J. Kamm, J.W. Kellogg, M.L. Kiefer, M.W. Kimmel, P.F. Knapp, M.D. Knudson, A. Kreft, G.R. Laity, P.W. Lake, D.C. Lamppa, W.L. Langston, J.S. Lash, K.R. LeChien, J.J. Leckbee, R.J. Leeper, G.T. Leifeste, R.W. Lemke, W. Lewis, S.A. Lewis, G.P. Loisel, Q.M. Looker, A.J. Lopez, D.J. Lucero, S.A. MacLaren, R.J. Magyar, M.A. Mangan, M.R. Martin, T.R. Mattsson, M.K. Matzen, A.J. Maurer, M.G. Mazarakis, R.D. McBride, H.S. McLean, C.A. McCoy, G.R. McKee, J.L. McKenney, A.R. Miles, J.A. Mills, M.D. Mitchell, N.W. Moore, C.E. Myers, T. Nagayama, G. Natoni, A.C. Owen, S. Patel, K.J. Peterson, T.D. Pointon, J.L. Porter, A.J. Porwitzky, S. Radovich, K.S. Raman, P.K. Rambo, W.D. Reinhart, G.K. Robertson, G.A. Rochau, S. Root, D.V. Rose, D.C. Rovang, C.L. Ruiz, D.E. Ruiz, D. Sandoval, M.E. Savage, M.E. Sceiford, M.A. Schaeuble, P.F. Schmit, M.S. Schollmeier, J. Schwarz, C.T. Seagle, A.B. Sefkow, D.B. Seidel, G.A. Shipley, J. Shores, L. Shulenburger, S.C. Simpson, S.A. Slutz, I.C. Smith, C.S. Speas, P.E. Specht, M.J. Speir, D.C. Spencer, P.T. Springer, A.M. Steiner, B.S. Stoltzfus, W.A. Stygar, J.W. Thornhill, J.A. Torres, J.P. Townsend, C. Tyler, R.A. Vesey, P.E. Wakeland, T.J. Webb, E.A. Weinbrecht, M.R. Weis, D.R. Welch, J.L. Wise, M. Wu, D.A. Yager-Elorriaga, A. Yu, E.P. Yu, Review of pulsed power-driven high energy density physics research on Z at Sandia, Phys Plasmas, 27, 070501 (2020).
[18] R.W. Lemke, M.D. Knudson, D.E. Bliss, K. Cochrane, J.-P. Davis, A.A. Giunta, H.C. Harjes, S.A. Slutz, Magnetically accelerated, ultrahigh velocity flyer plates for shock wave experiments, J Appl Phys, 98, 073530 (2005).
[19] L.M. Barker, R.E. Hollenbach, Laser interferometer for measuring high velocities of any reflecting surface, J Appl Phys, 43, 4669-4675 (1972).
[20] L.M. Barker, K.W. Schuler, Correction to the velocity-per-fringe relationship for the VISAR interferometer, J Appl Phys, 45, 3692-3693 (1974).
[21] S. Root, K.R. Cochrane, J.H. Carpenter, T.R. Mattsson, Carbon dioxide shock and reshock equation of state data to 8 Mbar: Experiments and simulations, Physical Review B, 87, 224102 (2013).
[22] S. Root, L. Shulenburger, R.W. Lemke, D.H. Dolan, T.R. Mattsson, M.P. Desjarlais, Shock Response and Phase Transitions of MgO at Planetary Impact Conditions, Phys Rev Lett, 115, (2015).
[23] G. Kresse, J. Hafner, Ab initio molecular dynamics for liquid metals, Physical Review B, 47, 558-561 (1993).
[24] G. Kresse, J. Hafner, Ab initio molecular-dynamics simulation of the liquid-metal--amorphous-semiconductor transition in germanium, Physical Review B, 49, 14251-14269 (1994).

[25] G. Kresse, J. Furthmüller, Efficient iterative schemes for ab initio total-energy calculations using a plane-wave basis set, Physical Review B, 54, 11169-11186 (1996).
[26] G. Kresse, J. Furthmüller, Efficiency of ab-initio total energy calculations for metals and semiconductors using a plane-wave basis set, Computational Materials Science, 6, 15-50 (1996).
[27] N.D. Mermin, Thermal Properties of the Inhomogeneous Electron Gas, Phys Rev, 137, A1441-A1443 (1965).
[28] J.P. Perdew, A. Ruzsinszky, G.I. Csonka, O.A. Vydrov, G.E. Scuseria, L.A. Constantin, X. Zhou, K. Burke, Restoring the Density-Gradient Expansion for Exchange in Solids and Surfaces, Phys Rev Lett, 100, 136406 (2008).
[29] P.E. Blöchl, Projector augmented-wave method, Physical Review B, 50, 17953-17979 (1994).
[30] H.J. Monkhorst, J.D. Pack, Special points for Brillouin-zone integrations, Physical Review B, 13, 5188-5192 (1976).
[31] A. van de Walle, P. Tiwary, M. de Jong, D.L. Olmsted, M. Asta, A. Dick, D. Shin, Y. Wang, L.Q. Chen, Z.K. Liu, Efficient stochastic generation of special quasirandom structures, Calphad, 42, 13-18 (2013).
[32] S. P. Lyon, J.D. Johnson, T-1 Handbook, the SESAME Equation of State Library, Los Alamos National Laboratory, Los Alamos, NM, , 1998.
[33] C. Kittel, Introduction to Solid State Physics Wiley Press, New York, pp. 704, 2005.
[34] P. Debye, Zur Theorie der spezifischen Wärmen, Annalen der Physik, 344, 789-839 (1912).
[35] J.D. Johnson, A generic model for the ionic contribution to the equation of state, High Pressure Res, 6, 277-285 (1991).
[36] S.L. Thompson, and Lauson, H S, Improvements in the CHART D radiation-hydrodynamic code III: revised analytic equations of state. United States: N. p., 1974. Web. , United States: N. p., 1974. Web. , DOI.
[37] A. Schmon, K. Aziz, G. Pottlacher, Density of liquid Ti-6Al-4V, EPJ Web Conf., 151, 04003 (2017).
[38] J.J.Z. Li, W.L. Johnson, W.-K. Rhim, Thermal expansion of liquid Ti–6Al–4V measured by electrostatic levitation, Appl Phys Lett, 89, 111913 (2006).
[39] CINDAS LLC, Global Benchmart for Critically Evaluated Materials Properties Data, https://cindasdata.com/Applications/TPMD/?
[40] F.D. Murnaghan, The Compressibility of Media under Extreme Pressures, Proc Natl Acad Sci U S A, 30, 244-247 (1944).
[41] G.I. Kerley, Equations of State for Titanium and Ti6Al4V Alloy, , in: SNL (Ed.) SAND Report #SAND2003-3785, Albuquerque, NM, 2003.
[42] T. Sjostrom, S. Crockett, S. Rudin, Multiphase aluminum equations of state via density functional theory, Physical Review B, 94, 144101 (2016).
[43] R.S. Hixson, J.N. Fritz, SHOCK COMPRESSION OF IRON**This work was supported by the US Department of Energy, in: S.C. Schmidt, R.D. Dick, J.W. Forbes, D.G. Tasker (Eds.) Shock Compression of Condensed Matter–1991, Elsevier, Amsterdam, pp. 69-70, 1992.
[44] S.D. Crockett, C.W. Greeff, J.D. Johnson, L. Burakovsky, Testing of a Liquid Equation of State Model Against Copper Data, AIP Conference Proceedings, 845, 65-68 (2006).
[45] P.F. Weck, P.E. Kalita, T. Ao, S.D. Crockett, S. Root, K.R. Cochrane, Shock compression of vanadium at extremes: Theory and experiment, Physical Review B, 102, 184109 (2020).
[46] G.I. Kerley, Kerley Technical Services Research Report KTS06-1, available at arXiv:1306.6916., 2006.
[47] J. Bouchet, F. Bottin, G. Jomard, G. Zérah, Melting curve of aluminum up to 300 GPa obtained through ab initio molecular dynamics simulations, Physical Review B, 80, 094102 (2009).

503 [48] A. Dewaele, V. Stutzmann, J. Bouchet, F. Bottin, F. Occelli, M. Mezouar, High pressure-
504 temperature phase diagram and equation of state of titanium, Physical Review B, 91, 134108
505 (2015).
506 [49] V. Stutzmann, A. Dewaele, J. Bouchet, F. Bottin, M. Mezouar, High-pressure melting curve of
507 titanium, Physical Review B, 92, 224110 (2015).
508 [50] A. Cezairliyan, J.L. McClure, R. Taylor, Thermophysical Measurements on 90Ti-6AI-4V Alloy
509 Above 1450 K Using a Transient (Subsecond) Technique, J. Res. Natl. Bur. Stand A 81A, 251 (1977).

510